Nanocomposites Based on CoSe₂-Decorated FeSe₂ Nanoparticles Supported on Reduced Graphene Oxide as High-Performance Electrocatalysts toward Oxygen Evolution Reaction

Guoxing Zhu,*[†] Xulan Xie,[†] Xiaoyun Li,[†] Yuanjun Liu,[‡] Xiaoping Shen,*[†] Keqiang Xu,[†] and Shaowei Chen*[§]

[†]School of Chemistry and Chemical Engineering, Jiangsu University, Zhenjiang 212013, China
[‡]School of Environmental and Chemical Engineering, Jiangsu University of Science and Technology, Zhenjiang 202018, China
[§]Department of Chemistry and Biochemistry, University of California, 1156 High Street, Santa Cruz, California 95064, United States

S *Supporting Information*

ABSTRACT: FeCo-based materials are promising candidates as efficient, affordable, and sustainable electrocatalysts for oxygen evolution reaction (OER). Herein, a composite based on FeSe₂@CoSe₂ particles supported on reduced graphene oxide (rGO) was successfully prepared as an OER catalyst. In the catalyst, the CoSe₂ phase was located on the FeSe₂ surface, forming a large number of exposed heterointerfaces with acidic iron sites because of strong charge interaction between CoSe₂ and FeSe₂. It is believed that the exposed heterointerfaces act as catalytic active sites for OER via a two-site mechanism, manifesting an overpotential as low as 260 mV to reach the current density of 10 mA cm⁻² in 1 M KOH and excellent stability for at least 6 h, which is superior to those of CoSe₂/rGO, FeSe₂/rGO, as well as most of the FeNi- and FeCo-based electrocatalysts reported in recent literatures. It was demonstrated that the most optimal composite electrocatalysts release more Fe species into the electrolyte during the OER process, whereas the releasing of Co species is negligible. When the FeSe₂@CoSe₂/rGO catalysts were loaded on a α-Fe₂O₃ photoanode, the photocurrent density was increased by three times. These results may open up a promising avenue into the design and engineering of highly active and durable catalysts for water oxidation.

KEYWORDS: *catalysis, composite materials, electrode, oxygen evolution reaction, heterointerfaces*
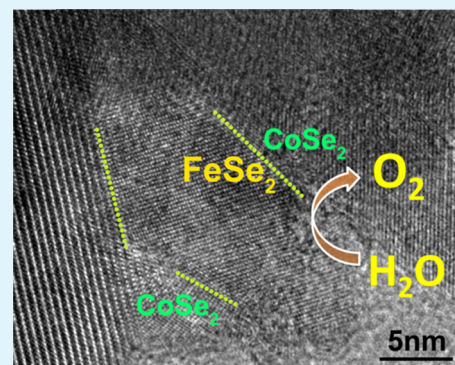
INTRODUCTION

Oxygen evolution reaction (OER; 4OH⁻ → O₂ + 2H₂O + 4e⁻ in base and 2H₂O → O₂ + 4H⁺ + 4e⁻ in acid) is an important half-reaction involved in many energy storage technologies, such as rechargeable metal−air batteries and solar H₂ fuel production from water splitting.[1−3] However, because of the sluggish electron-transfer kinetics, OER has been recognized as a major bottleneck that limits the overall efficiency of metal−air batteries and water splitting.[4−6] Traditionally, OER is catalyzed by noble metal-based materials such as Ru, RuO₂,[7] and IrO₂,[8] which often show high catalytic activity in acidic solution. However, their prohibitive cost and scarcity seriously limit their wide spread applications.

Thus, extensive research has been carried out to find alternative OER catalysts made of low-cost and earth-abundant materials. Among these, composites based on 3d transition metals such as iron, cobalt, and nickel have been attracting considerable attention.[9,10] Generally, Fe has very rich redox properties and is more earth-abundant and cheaper than other transition metals (and noble metals)[11,12] and thus attracts much attention for potential applications as various catalysts. Yet, iron

materials alone show only a low OER activity.[9] In contrast, Fe-based catalysts doped with additional metal ions such as nickel and cobalt show a much higher catalytic performance.[13−15] In these binary catalysts, it is believed that there is a strong interaction between Fe and the second metal sites such as Co²⁺ and Ni²⁺, leading to enhanced catalytic performance,[16,17] although the detailed mechanism, in particular, the catalytic active site, has remained elusive. Nevertheless, considering the synergistic effect between Fe and the second metal sites, OER catalysts with a homogeneous component distribution of the involved metal sites are generally preferred. Up to date, studies have largely focused on FeNi-[18,19] or FeCo-based[20,21] catalysts with homogeneous composition distribution. Very recently, homogeneous tertiary FeCoW-based hydroxide catalysts have also been prepared and show an excellent catalytic activity for OER.[21]

Anions may also impact the catalytic activity.[22,23] For instance, anions can influence the electrical conductivity of the catalysts. The interactions between anions and metal sites may significantly tune the geometric and electronic structures of the catalytic active sites, providing an opportunity for the design of highly efficient catalysts.[24,25] In fact, sulfide- or selenide-based materials have been prepared and exhibited effective activity for OER.[26−29] For example, Luo et al. prepared several typical FeNi-based or NiCo-based selenide micro-/nanostructures and demonstrated their high catalytic activity for OER.[30−33] Shen et al. used nitrogen-doped graphitic carbon as the substrate to prepare $Fe_{0.5}Co_{0.5}S$@N-doped carbon hybrid catalysts.[26] The hybridization of electrically conductive graphitic carbon with Co-doped FeS imparted strong heteroatomic interactions and hence high OER catalytic activity. In another study,[27] monoclinic $CoFe_2Se_4$ at different Co/Fe ratios was prepared and used as OER catalysts. The catalytic OER performance of Fe-doped $CoSe_2$ was also studied.[28] In these catalysts, Co and Fe were homogeneously mixed forming a solid solution.

Herein, a phase-separated composite consisting of $CoSe_2$, $FeSe_2$, and reduced graphene oxide (rGO) was prepared by using a simple solvothermal route. $FeSe_2$@$CoSe_2$ nanoparticles were dispersed on the rGO surface forming $FeSe_2$@$CoSe_2$/rGO composites. In the $FeSe_2$@$CoSe_2$ nanoparticles, $CoSe_2$ and $FeSe_2$ were phase-separated forming abundant exposed heterointerfaces, where $CoSe_2$ was mainly located on the $FeSe_2$ surface. In OER tests, an overpotential of only 260 mV was needed to reach the current density of 10 mA cm^{-2}, along with a small Tafel slope of 36 mV dec^{-1}, a large turnover frequency (TOF) of 0.13−0.86 s^{-1} based on cobalt sites at the overpotential of 0.35 V, and excellent stability for at least 6 h. This performance is much better than those of $CoSe_2$/rGO and $FeSe_2$/rGO catalysts prepared under similar conditions, suggesting a strong synergistic effect between $CoSe_2$ and $FeSe_2$. The catalytic active sites were most likely located at the heterointerfaces. The possible catalytic mechanism was proposed. When this catalyst was applied onto the Fe_2O_3 photoanode for photoelectrolysis-driven water splitting, the current density was increased by three times.

■ EXPERIMENTAL SECTION

Preparation of Graphene Oxide. The used graphene oxide (GO) was prepared from graphite powder with a modified Hummers' method.[34]

Preparation of FeSe$_2$/rGO and CoSe$_2$/rGO. FeSe$_2$/rGO hybrids were synthesized using GO, Fe(NO$_3$)$_3$, and Se powders as the precursors. GO (0.04 g) was first dispersed in distilled water (20 mL) with the assistance of sonication. Then, 1 mmol Fe(NO$_3$)$_3$·9H$_2$O and 23 mmol citric acid were added into the GO dispersion under vigorous stirring. Another solution containing 4 mmol Se powder and 15 mL of N$_2$H$_4$·H$_2$O was added into the above solution with a dropwise fashion under vigorous stirring. The obtained mixture was heated in a 95 °C oil bath. After being stirred overnight in the oil bath, the mixture was transferred to an autoclave and heated at 180 °C for 12 h. After cooling down naturally, the obtained solid was filtered, washed several times with deionized water, and dried at 60 °C for 12 h to obtain the final product, which was annealed at 450 °C for 1 h in an argon atmosphere. For comparison, FeSe$_2$ was also prepared without GO in a similar fashion. The CoSe$_2$/rGO sample was also prepared similarly by using an equivalent amount of CoCl$_2$·6H$_2$O instead of Fe(NO$_3$)$_3$·9H$_2$O.

Preparation of FeSe$_2$@CoSe$_2$/rGO. In a typical synthesis, CoCl$_2$·6H$_2$O (0.04 g) and polyvinylpyrrolidone (PVP, 0.075 g) were dissolved in 80 mL of N,N-dimethyl formamide (DMF). FeSe$_2$/rGO

(0.06 g, prior to annealing at 450 °C) was dispersed in the solution under stirring and sonication. After that, the mixture was loaded into a Teflon-lined stainless steel autoclave and heated at 180 °C for 30 h. The obtained solid was collected by centrifugation, washed with water, and dried under vacuum at 60 °C. Finally, the obtained solid product was also annealed at 450 °C for 1 h in argon atmosphere. The final obtained sample was denoted as FeSe$_2$@CoSe$_2$/rGO-2. FeSe$_2$@CoSe$_2$/rGO-1 and FeSe$_2$@CoSe$_2$/rGO-3 were prepared in the same manner except that the amount of added CoCl$_2$·6H$_2$O was 0.02 and 0.06 g, respectively.

Preparation of Co/rGO. Briefly, CoCl$_2$·6H$_2$O (0.04 g) and PVP (0.075 g) were dissolved into the same GO dispersion obtained with 0.04 g of GO and 40 mL of DMF. The obtained mixture was loaded into Teflon stainless steel autoclaves, maintaining at 180 °C for 30 h. The formed solid powder was then collected, washed, and annealed with the same procedure as that of FeSe$_2$@CoSe$_2$/rGO-2. The final obtained sample was denoted as Co/rGO.

Preparation of an α-Fe$_2$O$_3$-Based Photoanode. An α-Fe$_2$O$_3$-based photoanode was prepared on FTO substrates according to a reported route,[35] which involves two steps: synthesis of FeOOH on FTO substrates and formation of α-Fe$_2$O$_3$ by subsequent annealing process.

Material Characterizations. Crystal phase characterization of the synthesized products was performed by using powder X-ray diffraction (XRD, Bruker D8 Advanced diffractometer, Cu Kα, λ = 1.5418 Å). The microstructure, morphology, and size analyses were conducted on a field emission scanning electron microscope (Hitachi S4800) and a transmission electron microscope (TEM, JEM-2010 or Tecnai G2 F30 S-TWIN). The elemental mapping analysis was also conducted on the TEM (Tecnai G2 F30 S-TWIN). The chemical states of the elements in the samples before or after OER testing were examined by X-ray photoelectron spectroscopy (XPS) measurements (Thermo ESCA-LAB 250, Al Kα radiation source, $h\nu$ = 1486.6 eV). The Raman spectra of the samples were carried out on a JY HR-800 Raman spectrometer with 453 nm laser excitation. The metal ion contents in the composites or the electrolyte during the OER process were determined by an inductively coupled plasma optical emission spectrometer (ICP−OES, Vista-MPX).

Loading of the Catalyst on the α-Fe$_2$O$_3$ Photoanode. A FeSe$_2$@CoSe$_2$/rGO-2 catalyst (2 mg) and a 5 wt % Nafion solution (10 μL) were dispersed in 1 mL of ethanol under sonication for at least 30 min to form a homogeneous mixture. Then, several microliters of the mixture (50 μL is the optimized amount) were cast onto the 1 × 1 cm^2 FTO-supported α-Fe$_2$O$_3$ photoanode, which was then left to dry in air. The obtained composite photoanode was denoted as α-Fe$_2$O$_3$//FeSe$_2$@CoSe$_2$/rGO-2.

Electrochemical Characterizations. Electrochemical studies were performed using a three-electrode system with a CHI 760D electrochemical workstation. A platinum wire and a Ag/AgCl electrode (with saturated KCl) were used as the counter electrode and reference electrode, respectively. The working electrode is a glassy carbon electrode (GCE) cast with catalyst powders. Before casting by catalyst powders, the GCE was polished by the α-alumina oxide powder (0.05 μm). To prepare the working electrode, 2 mg of catalyst, 3.5 mg of acetylene black, and 10 μL of a 5 wt % Nafion solution were dispersed in 1 mL of ethanol under sonication for at least 30 min to form a homogeneous mixture. Then, 5 μL of the mixture was drop-cast onto the GCE surface and dried in air. The catalyst loading was determined to be about 0.14 mg cm^{-2}.

The potential value was converted into that versus RHE based on the following formula, $E_{RHE} = E_{Ag/AgCl} + E^\circ_{Ag/AgCl} + 0.059$ pH (in volts). The electrolyte is 1 M KOH solution. Cyclic voltammetric scanning was first performed at the scanning rate of 500 mV s^{-1} for 500 cycles. After that, cyclic voltammograms were collected at various scan rates (e.g., 20, 40, 60, 80, and 100 mV s^{-1}) to detect the electrochemical surface of the catalysts. Tafel slopes were derived from the linear sweep voltammetry (LSV) curves by plotting overpotential (η) against log(J). The stability test was performed with 1000 CV cycles between 0.2 and 0.7 V (vs Ag/AgCl) at the sweep rate of 50 mV s^{-1}. At the end of the cycling test, polarization curves were collected with the sweep

Scheme 1. Schematic Illustration of the Preparation of the FeSe$_2$@CoSe$_2$/rGO Composite by Two Solvothermal Steps
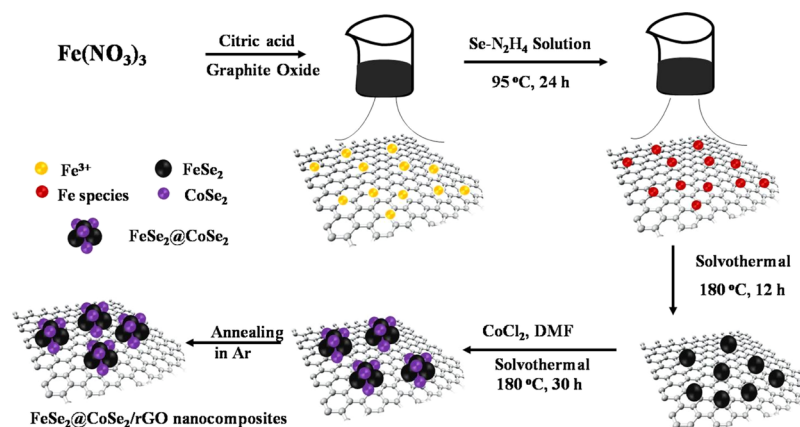
rate of 5 mV s^{-1}. The amperometric (i–t) curves were also recorded at a constant potential to evaluate the catalyst stability. The catalyst after OER testing (2000 cycles between 0.2 and 0.7 V vs Ag/AgCl) was also investigated by XRD and XPS to check the change of the catalyst during the OER process. For the investigation of photoelectrochemical (PEC) water-splitting performance of the composite photoanode (α-Fe$_2$O$_3$//FeSe$_2$@CoSe$_2$/rGO-2), 1 M KOH solution was used as the electrolyte; A 300 W Xe lamp was used to provide the light.

The values of TOF are calculated by assuming that all cobalt or iron ions in the catalysts are active and contribute to the catalytic reaction (lowest TOF values were calculated), TOF = $jS/(4Fn)$. Here, j (mA cm^{-2}) is the measured current density at η = 0.35 V; S (0.0707 cm^2) is the surface area of the GCE; the number of 4 means 4 electrons per O$_2$ molecular; F is the Faraday constant (96485.3 C mol^{-1}); and n is the Co or Fe ion molar number calculated from the catalyst loading density.

Faradaic Efficiency. A rotating ring-disk electrode (RRDE) was used to test the Faradaic efficiency during the OER process with the FeSe$_2$@CoSe$_2$/rGO-2 catalyst. The collection efficiency of the RRDE was tested according to a reported method.[36] The collection efficiency value is the ratio of the ring current and the disk current in the electrolyte of 0.01 M K$_3$[Fe(CN)$_6$] and 0.1 M NaOH, which are collected in the positive sweep direction (20 mV s^{-1}) and at a constant ring potential of 1.55 V versus RHE. The potential of 1.55 V is selected because with this ring potential, the Fe(II) species produced at the disk electrode can be oxidized into Fe(III) on the ring electrode.[37] The tested collection efficiency of our RRDE is 0.38 with rotation rates of 100–2500 rpm. To detect the Faradaic efficiency of different catalysis reaction times with our FeSe$_2$@CoSe$_2$/rGO-2 catalyst, the applied potential on the disk electrode is held at 260 mV versus RHE (under this potential, a current density of 10 mA cm^{-2} can be obtained). The ring current was collected under 280 mV versus RHE every 10 min to check the Faradaic efficiency change with the catalytic process. The Faradaic efficiency was calculated according to

$$\text{Faradaic efficiency} = \frac{n_{app} \times i_r}{N \times i_d}$$

where N is the collection efficiency, i_r and i_d are the ring and disk currents. n_{app} is calculated as 2.[38] It should be mentioned that because only dissolved O$_2$ can be reduced on the ring electrode, thus the measured Faradaic efficiency is much lower than the actual value due to many undissolved oxygen bubbles,[36,38] especially under the case with higher current density or higher overpotential.

■ RESULTS AND DISCUSSION

Synthesis and Characterization. The synthesis procedure for FeSe$_2$@CoSe$_2$/rGO is illustrated in Scheme 1. The FeSe$_2$/rGO hybrid was first prepared via a solvothermal route by using Fe(NO$_3$)$_3$·9H$_2$O, Se powder, and GO as precursors. In the

synthesis, citric acid was used because it could coordinate with Fe^{3+} ions forming a complex to modulate the reaction kinetics. In addition, the residual citric radical ions can be easily removed by annealing at temperature higher than 175 °C.[39] N$_2$H$_4$·H$_2$O was used as a reducing agent, reducing Fe(III) to lower oxidation state, Se to Se$_x^{2-}$, and GO to rGO. The resultant Se$_x^{2-}$ ions then bond with Fe species forming FeSe$_2$. To load CoSe$_2$ onto FeSe$_2$, the FeSe$_2$/rGO hybrid was dispersed in a DMF solution containing Co^{2+}, as cobalt ions selectively adsorbed on the surface of FeSe$_2$ because of the strong interactions between selenium species and cobalt ions. Hydrothermal heating led to the partial conversion from FeSe$_2$ to CoSe$_2$, forming FeSe$_2$@CoSe$_2$ composite with abundant heterointerfaces, in which CoSe$_2$ was located on the FeSe$_2$ surface. The final catalyst was obtained by annealing the formed product at 450 °C for 1 h in an argon atmosphere to remove residual organic impurities and enhance crystallinity of the FeSe$_2$@CoSe$_2$ solid and interfacial contact between different components. It should be noted that the temperature of 450 °C was selected because it is high enough to remove residual citric acid, whereas at higher temperatures (such as 600 °C), FeSe$_2$ will discompose to form Se powders.

The crystal phases of the formed composites were first investigated by powder XRD measurements. The diffraction patterns of FeSe$_2$/rGO (Figure 1) are consistent with those of pristine FeSe$_2$ with the ferroselite phase. The diffraction peaks at 2θ = 24.1°, 31.1°, 34.8°, 36.2°, 48.2°, 50.9°, 53.9°, and 64.1° can be indexed to the (110), (101), (111), (120), (211), (002), (031), and (112) planes of ferroselite phase FeSe$_2$ (JCPDS no. 79-1892, orthorhombic phase, *Pnnm*, a cell size of 0.4804 × 0.5784 × 0.3586 nm). Similar diffraction patterns were observed with the FeSe$_2$@CoSe$_2$/rGO-1 sample, whereas some additional peaks emerged in FeSe$_2$@CoSe$_2$/rGO-2 and FeSe$_2$@CoSe$_2$/rGO-3 at 2θ = 30.3°, 34.2°, 37.5°, 43.6°, 51.6°, 56.5°, and 58.9°. These diffraction peaks can be indexed to cubic CoSe$_2$ (JCPDS no. 88-1712, cubic phase, *Pa-3*, a cell size of 0.5859 × 0.5859 × 0.5859 nm), in agreement with those of CoSe$_2$/rGO. In addition, the relative intensity of the CoSe$_2$ diffraction peaks increases gradually from FeSe$_2$@CoSe$_2$/rGO-1 to FeSe$_2$@CoSe$_2$/rGO-3, suggesting an increase of CoSe$_2$ loading in the FeSe$_2$@CoSe$_2$/rGO composites. For comparison, the XRD pattern of the formed Co/rGO-450 product was also shown, which can be attributed to cubic metallic Co (JCPDS no. 01-1259).

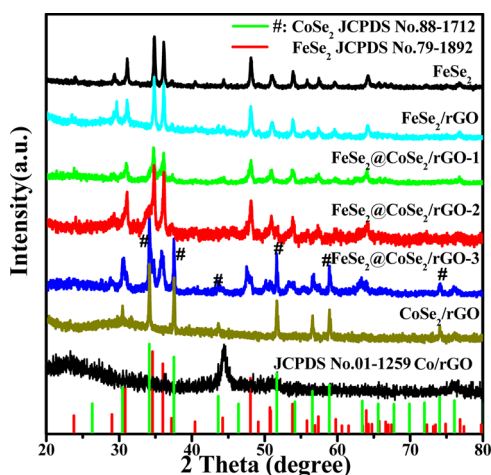XPS analysis was then carried out to determine the chemical composition and oxidation state of the prepared FeSe$_2$@CoSe$_2$

Figure 1. XRD patterns of FeSe₂, FeSe₂/rGO, and FeSe₂@CoSe₂/rGO prepared with different cobalt dosages, CoSe₂/rGO, and Co/rGO. For comparison, the standard patterns of CoSe₂ (JCPDS no. 88-1712) and FeSe₂ (JCPDS no. 79-1892) are also shown.

hybrids. The Co, Fe, Se, C, and O elements can be readily identified in the composites from the full survey scan (Figure S1a, see the Supporting Information), where the small signals of nitrogen come from DMF used as a solvent for the synthesis). In the high-resolution scan of the C 1s electrons, deconvolution yields a major peak at 284.6 eV for sp² C=C and minor ones for C=O (284.9 eV) and C–O (285.8 eV) (Figure S1b).[40]

Figure 2a depicts the high-resolution spectra of Fe 2p electrons in the series of samples. The sharp band at 706.3 eV may be indexed to the 2p₃/₂ electrons of metallic Fe(0). The bands at 710.6 and 725.0 eV correspond to the Fe 2p₃/₂ and Fe 2p₁/₂ electrons of Fe(III) or Fe(II),[41] respectively, along with a satellite peak at 719.2 eV. These XPS features are typical of Fe species in an octahedral configuration.[42] Interestingly, after the loading of CoSe₂, the intensity of the 706.3 eV peak decreased, whereas that of the wide peak in the range of 715−708 eV increased. The latter might be deconvoluted into two subpeaks, corresponding to two different chemical environments of the Fe sites. The one at higher binding energy (about 713.2 eV) increased in intensity with increased CoSe₂ loading, suggesting that more iron species at a higher oxidation state are formed after CoSe₂ loading.

The high-resolution spectra of Co 2p are shown in Figure 2b. All samples show two main bands at 785−776 and 800−792

eV, corresponding to the Co 2p₃/₂ and Co 2p₁/₂, respectively. The Co 2p₃/₂ band can be deconvoluted into two peaks centered at 780.8 and 778.2 eV for CoSe₂/rGO, which shifted to lower binding energy in the FeSe₂@CoSe₂/rGO composite (Figure 2b). The fact that the Co binding energy was lower in FeSe₂@CoSe₂/rGO than that in CoSe₂/rGO, whereas more iron species at higher binding energy in the former suggests electron transfer from the Fe sites to the Co sites. Meanwhile, two satellite peaks (786.2 and 802.8 eV) can be seen at the higher energy side of the Co 2p peak, likely because of the antibonding orbital between the Co and Se atoms.[43] This implies that Co²⁺ in CoSe₂ entailed a d⁷ electronic configuration in the form of $t_{2g}^6 e_g^1$, which is close to the optimal e_g filling of 1.2 for a paramagnetic configuration that is believed to be desired for high-performance electrocatalysts.[44]

In addition, the Se 3d₅/₂ and Se 3d₃/₂ electrons can be identified at 54.3 and 55.2 eV, respectively (Se−Se) (Figure S1c, see the Supporting Information), which are consistent with bulk selenides.[45,46] Both CoSe₂/rGO and FeSe₂@CoSe₂/rGO-3 show almost the same binding energy for Se 3d, suggesting that the FeSe₂@CoSe₂/rGO-3 sample was fully covered with CoSe₂. In the samples of FeSe₂/rGO, FeSe₂@CoSe₂/rGO-1, FeSe₂@CoSe₂/rGO-2, these two Se 3d bands shifted to 54.0 and 54.7 eV, suggesting different Se chemical environments. The band at 58−61 eV can be indexed to the overlap of Se 3d in SeOₓ and the Co 3p band (Figure S1c, see the Supporting Information).[47]

Raman measurements were conducted to characterize rGO in the product (Figure S2, see the Supporting Information). The characteristic D (1350 cm⁻¹) and G (1590 cm⁻¹) bands of carbon materials are clearly observed,[48] suggesting the presence of rGO in the final products. It was found that the I_D/I_G ratios slightly increased as the cobalt content increased, from 1.54 for FeSe₂/rGO to 1.57, 1.62, and 1.66 for FeSe₂@CoSe₂/rGO-1, FeSe₂@CoSe₂/rGO-2, and FeSe₂@CoSe₂/rGO-3, respectively. This phenomenon is similar to other Co-based graphene composites.[49] The increase of D peak intensity may be ascribed to the interaction between CoSe₂ and rGO.

SEM and TEM measurements were carried out to examine the size, morphology, and microstructure of the formed FeSe₂@CoSe₂/rGO composites. From the SEM and TEM images (Figure S3, see the Supporting Information), one can see that FeSe₂ particles aggregated into ensembles of 100−500 nm and were loaded on graphene nanosheets in FeSe₂/rGO. For FeSe₂@CoSe₂/rGO-2 (Figure S4, see the Supporting Information), the particles showed a wide size distribution in the range of several tens of nanometers to hundreds of
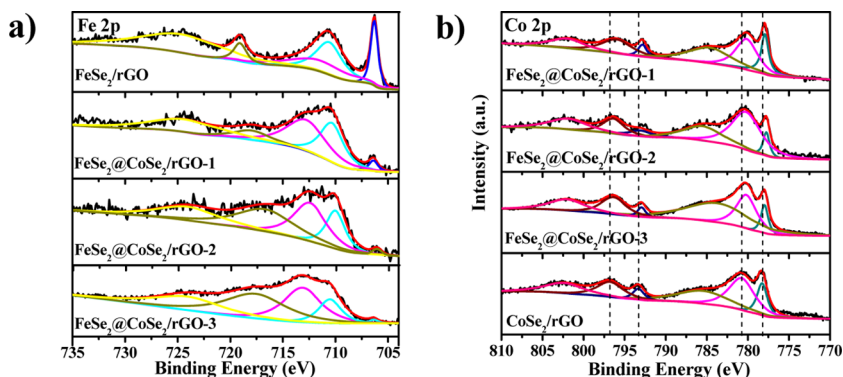

Figure 2. High-resolution XPS spectra of CoSe₂/rGO, FeSe₂/rGO, and FeSe₂@CoSe₂/rGO products. (a) Detailed Fe 2p and (b) detailed Co 2p.

nanometers. The size change might be due to the reaction of $FeSe_2$ with Co^{2+} that caused the disintegration of $FeSe_2$ aggregates into smaller ones. Figure 3 shows the TEM images
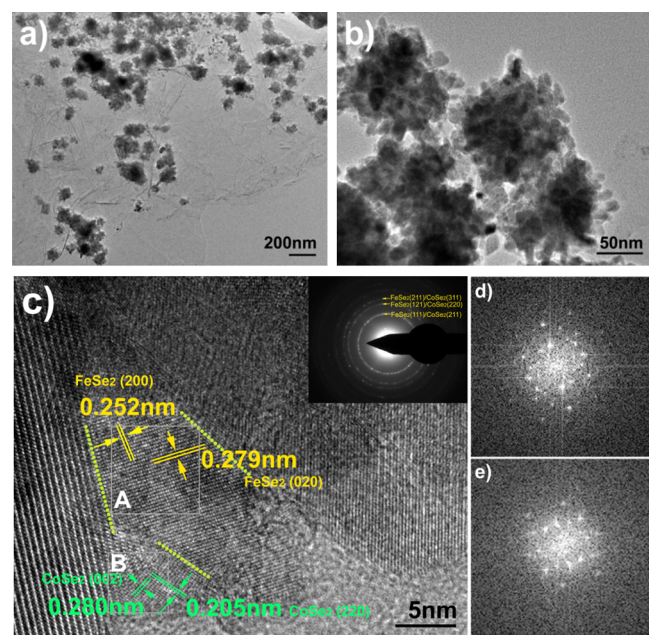

Figure 3. TEM analysis of the $FeSe_2@CoSe_2/rGO-2$ composites. (a,b) Low-magnification TEM images and (c) HRTEM image suggesting the formation of separated phases of $FeSe_2$ and $CoSe_2$. The inset of (c) shows the SAED pattern recorded on one of the composite particles. (d,e) Corresponding fast Fourier-transformed (FFT) patterns for the noted areas of (A,B) in (c), respectively.

of the $FeSe_2@CoSe_2/rGO-2$ composite. One can see that spherical particles of 50−80 nm are loaded on the graphene nanosheet surface and the particles are composed of small rodlike particles, forming a porous structure, as further manifested in the observation with scanning transmission model (STEM, Figure 4a). In addition, well-defined lattice fringes can be observed in high-resolution TEM (HRTEM) images, where the FFT patterns suggests the coexistence of phase-separated orthorhombic $FeSe_2$ and cubic $CoSe_2$ (Figure 3c−e), forming abundant heterointerfaces between $FeSe_2$ and

$CoSe_2$ (highlighted by the dotted lines). The lattice fringes with interplanar distances of 0.279 and 0.252 nm are corresponding to the (020) and (200) crystal planes of orthorhombic $FeSe_2$; whereas those with interplanar distances of 0.280 and 0.205 nm to the (002) and (220) crystal planes of cubic $CoSe_2$. The inset of Figure 3c shows the selected-area electron diffraction (SAED) pattern recorded on one of the composite particles, which demonstrates the ringlike diffraction pattern. These diffraction rings can be indexed into the overlap of $FeSe_2$ and $CoSe_2$ because of their close crystal plane spacings.

EDX analysis on the composite further validates the existence of Fe, Co, Se, C, and O elements in the composite (Figure 4b). Elemental mapping analysis (Figure 4c−f) shows that the Fe, Co, and Se elements are uniformly distributed on the randomly selected particle, whereas Se and Co can be found in a slightly bigger area than Fe, consistent with the loading of $CoSe_2$ species on the $FeSe_2$ surface.

Electrochemical Characterization. The OER activities of the prepared products are then investigated with a standard three-electrode system in a KOH aqueous solution. For comparison, the blank GCE, commercial RuO_2, and Pt/C were also investigated under the same condition (see details in the Experimental Section). Figure 5 shows the LSV curves in 1 M KOH. It can be seen that the $FeSe_2@CoSe_2/rGO-2$ sample demonstrates the lowest onset potential of 1.45 V (defined as the potential at a current density of 0.1 mA cm^{-2})[50] for water oxidation. The overpotential to reach a current density of 10 mA cm^{-2} (η_{10}) is also different among the samples.[51] Notably, the η_{10} values of $FeSe_2@CoSe_2/rGO$ are all lower than those of RuO_2 (η_{10} of 380 mV) and Pt/C (η_{10} of 435 mV). For instance, η_{10} was only 260 mV for $FeSe_2@CoSe_2/rGO-2$, 278 mV for $FeSe_2@CoSe_2/rGO-1$, and 312 mV for $FeSe_2@CoSe_2/rGO-3$ (Figure 5c), exhibiting a unique "V-type" plot with the cobalt content. Note that the $FeSe_2/rGO$ (η_{10} of 475 mV), $CoSe_2/rGO$ (η_{10} of 370 mV), and Co/rGO (η_{10} of 455 mV) samples exhibited much weak OER activities than $FeSe_2@CoSe_2/rGO$, suggesting a strong synergistic effect between Fe and Co compositions causing enhanced catalytic activity, and $FeSe_2@CoSe_2/rGO-2$ represents the best catalyst within the present experimental context.

Further analysis was carried out with the Tafel plots (Figure 5b), which were calculated by using the LSV curves according to the Tafel equation $\eta = b \log j + a$, where j is the current
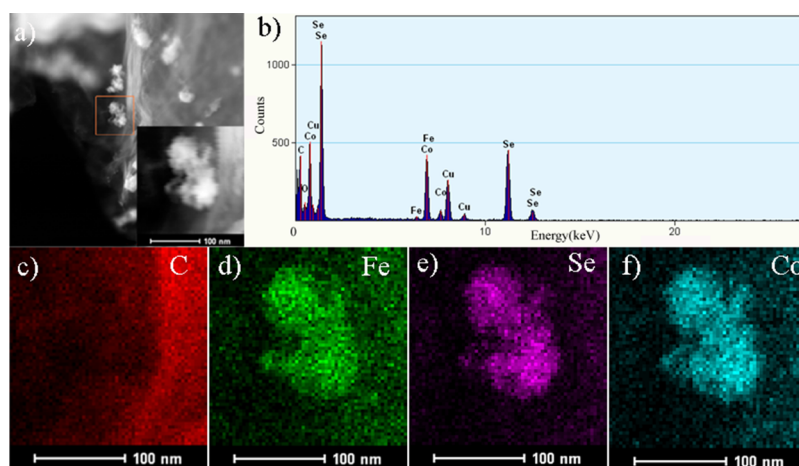

Figure 4. Elemental mapping analysis of the $FeSe_2@CoSe_2/rGO-2$ product. (a) STEM image and (b) energy-dispersive X-ray (EDX) profile. The corresponding elemental mapping for (c) carbon, (d) iron, (e) selenium, and (f) cobalt of the selected area shown in the inset of (a).
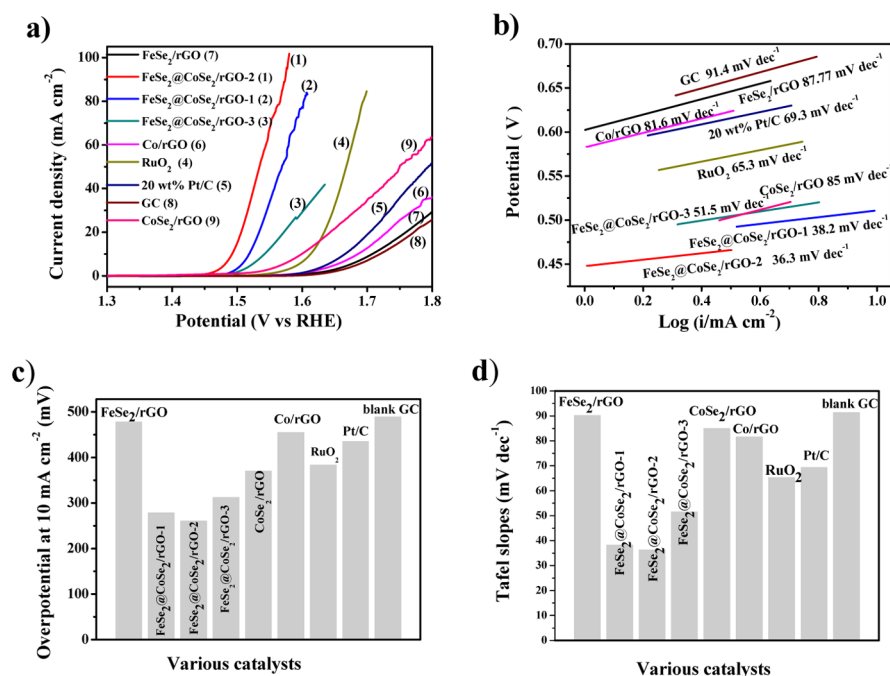
Figure 5. (a) LSV curves (after *iR*-compensated) obtained with various catalysts including FeSe₂/rGO, FeSe₂@CoSe₂/rGO-1, FeSe₂@CoSe₂/rGO-2, FeSe₂@CoSe₂/rGO-3, CoSe₂/rGO, Co/rGO, RuO₂, Pt/C, and blank GC tested in 1 M KOH. (b) Corresponding Tafel plots in the linear region. (c) Overpotential values at 10 mA cm⁻² and (d) Tafel slopes for various catalysts.
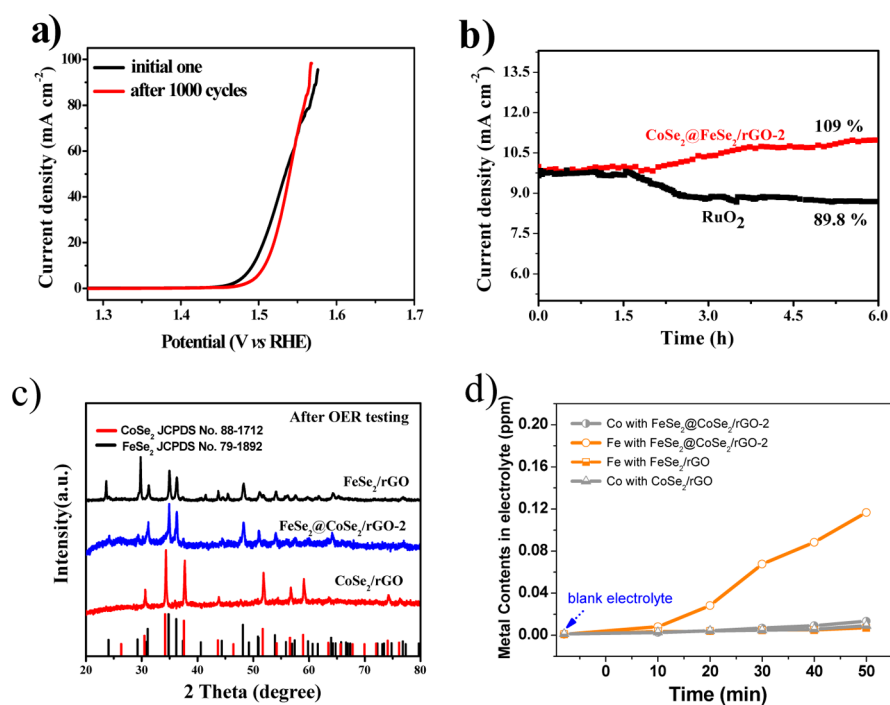

Figure 6. (a) OER polarization curves for the FeSe₂@CoSe₂/rGO-2 composite before and after 1000 cycles and (b) amperometric (*i–t*) curves were recorded at a constant applied potential (260 mV vs RHE) to evaluate the stability of the catalysts. (c) XRD patterns of the products of FeSe₂/rGO, FeSe₂@CoSe₂/rGO-2, and CoSe₂/rGO after OER testing. Standard patterns of CoSe₂ (JCPDS no. 88-1712) and FeSe₂ (JCPDS no. 79-1892) are also shown. (d) Fe and Co ion contents in the electrolyte tested by the ICP−OES method as a function of electrocatalysis time for the three contrast catalysts, CoSe₂/rGO, FeSe₂@CoSe₂/rGO-2, and FeSe₂/rGO.

density and *b* is the Tafel slope. FeSe₂@CoSe₂/rGO-2 shows the lowest Tafel slope (36 mV dec⁻¹) among the samples, much lower than those of FeSe₂/rGO (87.8 mV dec⁻¹), CoSe₂/rGO (85 mV dec⁻¹), and Co/rGO (81.6 mV dec⁻¹), suggesting a high intrinsic activity of FeSe₂@CoSe₂-based composites. This suggests that the synergistic interactions between FeSe₂

and CoSe₂ might modify the electronic structure of the catalyst active sites and thus provide excellent electrocatalytic OER activity.[52,53] The Tafel slope not only indicates the current density changes with increasing overpotential but also contains important information about the reaction mechanism including the possible rate-determining step in the four electron-/proton-
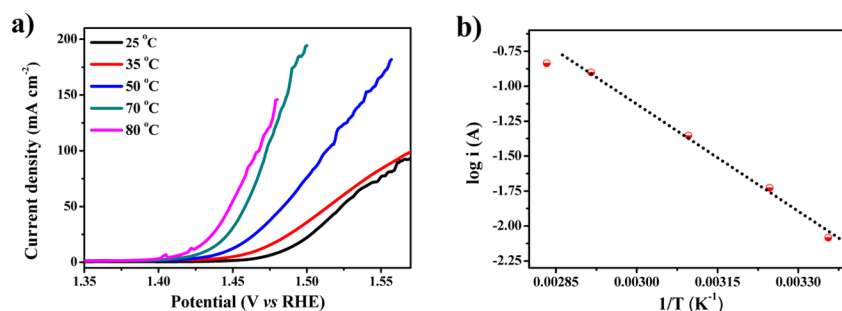
Figure 7. (a) OER polarization curves of FeSe$_2$@CoSe$_2$/rGO-2 in 1 M KOH aqueous electrolyte at 25, 35, 50, 70, and 80 °C. (b) Arrhenius plot of the kinetic current at η = 260 mV without *iR* correction.

transfer steps of OER.[54] According to the classical Butler−Volmer formalism, a Tafel slope near 40 mV dec^{-1} implies that the second electron transfer in OER is rate-determining and a slope near 24 mV dec^{-1} implies that the third electron transfer is rate-determining. In our case, we note that in Figure 5d, there is a near-continuous change in the slope (decreasing from 87.8 to 36.3 mV dec^{-1} and then increasing to 85 mV dec^{-1}) as a function of Co content. This change trend is quite similar to that observed with Co$_{1-x}$Fe$_x$(OOH) catalysts[52] and suggests that the Butler−Volmer mechanistic kinetics may not be sufficient to describe the OER in this case. The two optimized catalysts, FeSe$_2$@CoSe$_2$/rGO-1 and FeSe$_2$@CoSe$_2$/rGO-2, present the Tafel slope values of 38.2 and 36.3 mV dec^{-1}, respectively. These may indicate that the possible rate-determining step for these two composite catalysts would be the second electron transfer in OER.[54] It should also be noted that the Tafel slope is a composite parameter, which can be influenced by many factors. The different Tafel slope values are also explainable by material-specific site interaction energies and probabilities (or rates) of dynamic active-site formation.[55]

To examine the impacts of pH on the OER activity,[56] we then investigated the catalytic activity of FeSe$_2$@CoSe$_2$/rGO-2 in 0.1 M of KOH (Figure S5a, see the Supporting Information). The samples of Pt/C and RuO$_2$ were also measured. It can be seen that the η_{10} values were all higher than those in 1 M KOH. For example, η_{10} was 335 mV for FeSe$_2$@CoSe$_2$/rGO-2 in 0.1 M KOH, 75 mV higher than that (260 mV) in 1 M KOH. The corresponding Tafel plot was also greater at 57.7 mV dec^{-1}, in contrast to 36 mV dec^{-1} in 1 M KOH (Figure S5b, see the Supporting Information). Notably, this Tafel slope remained lower than those of RuO$_2$ and Pt/C in the same solution. These results suggest that FeSe$_2$@CoSe$_2$/rGO-2 exhibited excellent OER activity both in 1 M KOH and 0.1 M KOH.

Table S1 shows the results of relevant catalysts reported in recent literatures. It can be seen that the catalytic activity of the FeSe$_2$@CoSe$_2$ sample was better than or comparable to those of other FeCo-, FeNi-, or NiCo-based catalysts such as Co-doped NiSe$_2$ nanoparticles (η_{10} = 390 mV in 1 M KOH),[57] CoFe-LDH/rGO (325 mV in 0.1 M KOH),[53] porous (Ni$_{0.75}$Fe$_{0.25}$)Se$_2$ nanosheets (255 mV in 1 M KOH),[58] (Ni, Co)$_{0.85}$Se product (255 mV in 1 M KOH),[47] and so forth.

The stability of the FeSe$_2$@CoSe$_2$/rGO-2 catalyst was then probed by continuing cycling (Figure 6a). The η_{10} value increased by 16 mV after 1000 cycles. Interestingly, at potentials higher than 1.55 V, a high current density remained after 1000 cycles. The long-term electrochemical stability of the catalyst was further tested with amperometric (*i*−*t*) measurements (Figure 6b). The current density at the overpotential of 260 mV increased slightly from 10 to 10.9 mA cm^{-2} (109%)

after 6 h of continuing operation. The stability test was also conducted on the RuO$_2$ catalyst, which shows a degradation of 10.2% after 6 h. The results suggest the remarkable stability of FeSe$_2$@CoSe$_2$/rGO-2 for OER. As shown in Figure 6b, there is a slight fluctuation in the *i*−*t* curve. The Faraday efficiency change of the catalyst during the OER process was then investigated by a RRDE (Figure S6, see the Supporting Information), which does not show obvious change. Thus, it is proposed that the slight current fluctuation during *i*−*t* testing may be caused by the disturbing of amounts of oxygen bubbles.

It is known that various OER catalysts are often oxidized during the OER process because of the used higher potential. In fact, it is widely believed that for metal-containing OER catalysts, the actual catalytic active phase is the surface in situ generated metal oxide or MOOH species because under the higher potential for OER, the surface metal sites will be oxidized, whereas the anions influence the electron structure of the metal sites and conductivity and thus can modify catalytic activity. To further evaluate the stability of our selenide catalysts, XRD and XPS investigation of the catalysts after OER testing (2000 cycles) was then carried out to check the possible oxidation or transform of these selenide catalysts. XRD patterns of the three contrast catalysts, CoSe$_2$/rGO, FeSe$_2$@CoSe$_2$/rGO-2, and FeSe$_2$/rGO after OER testing are shown in Figure 6c, which show almost the same pattern as those without experiencing OER testing. This suggests that the catalyst bulk did not have phase change during the OER process, whereas the possible oxidation or composition losing of the catalysts may only occur on their surface. XPS results of the three catalysts (CoSe$_2$/rGO, FeSe$_2$@CoSe$_2$/rGO-2, and FeSe$_2$/rGO) after OER testing are shown in the Supporting Information (Figures S7−S9). Comparing the XPS spectra before (Figures 2 and S1, see the Supporting Information) and after (Figures S7−S9, see the Supporting Information) OER testing, it was found that after OER testing, the Fe 2p binding energy of FeSe$_2$@CoSe$_2$/rGO-2 and FeSe$_2$/rGO products has an obvious blue shift, especially for the band at lower binding energy. As for the Co 2p band of CoSe$_2$/rGO and FeSe$_2$@CoSe$_2$/rGO-2 products, the original XPS band at ~778.3 eV disappears after OER testing, only leaving the band at higher binding energy of 780.8 eV. All of these suggest that both Fe and Co species on the catalyst surface are oxidized during the OER process. In addition, the Se XPS band (53−57 eV) in the three samples also presents a similar blue shift after OER testing.

The metal ion content in the electrolyte during the OER process was also measured to check the possible dissolve of the catalyst (Figure 6d). The results exhibit that the content of Fe species in the electrolyte gradually increasing, whereas the dissolve of Co species during the OER process is relatively

Table 1. Comparison of OER Activity Data and Specific Surface Area for the Investigated Catalysts

catalysts	η_{10}[a] [mV]	mass activity at $\eta = 350$ mV[b] [A g^{-1}]	TOF$_{Co}$ at $\eta = 350$ mV[c] [S^{-1}]	TOF$_{Fe}$ at $\eta = 350$ mV[c] [S^{-1}]	S_{BET} [m^2 g^{-1}]	specific activity at $\eta = 350$ mV[d] [mA cm^{-2}]	C_{dl} [mF cm^{-2}]
FeSe$_2$/rGO	478	3.84		0.0023	6.72	0.057	0.05
FeSe$_2$@CoSe$_2$/rGO-1	278	445.0	0.865	0.351	12.6	3.54	0.42
FeSe$_2$@CoSe$_2$/rGO-2	260	727.1	0.661	0.588	22.9	3.18	1.15
FeSe$_2$@CoSe$_2$/rGO-3	312	164.8	0.128	0.135	23.3	0.71	0.35
CoSe$_2$/rGO	370	47.5	0.028		6.61	0.72	0.75

[a]The overpotential at the current density of 10 mA cm^{-2} for the catalysts. [b]Specific activity is normalized to the mass loading. [c]See the Experimental Section for the calculation method. [d]The values of specific activity (mA cm^{-2}) are calculated from the BET surface area S_{BET} (m^2 g^{-1}), the catalyst loading density m (0.14 mg cm^{-2}), and the measured current density j (mA cm^{-2}) at $\eta = 0.35$ V with the formula of specific activity = $j/(10S_{BET}m)$.

weak. This is similar to that of the Co$_{1-x}$Fe$_x$(OOH) catalyst investigated by Boettcher et al., that is, Fe species is easily dissolved into the electrolyte.[52] In that case, they found that the Co$_{1-x}$Fe$_x$(OOH) film can lose 18−44% of the mass after 2 h OER process.[52] It was also found by Danilovic et al. that the most active materials for OER are often with the weakest stability.[59] Thus, as argued by Danilovic et al., it is very important to consider the balance between high activity and high stability for a best OER catalyst.[59]

To assess the kinetic barriers involved in OER, we studied the effect of temperature on the OER performance of the FeSe$_2$@CoSe$_2$/rGO-2 composite (Figure 7a). It can be seen that the onset potential decreases with the increase of reaction temperature. That is, the OER proceeds more rapidly at higher temperatures.[60] From an Arrhenius fit

$$\frac{\partial \log(i)}{\partial (1/T)} = -\frac{E_a}{2.303R}$$

with data acquired at $\eta = 260$ mV, the apparent electrochemical activation energy was estimated to be 46.3 kJ/mol for the FeSe$_2$@CoSe$_2$/rGO-2 catalyst. This value is smaller than or comparable to those of leading OER catalysts such as FeCoW-based catalyst (49 kJ/mol),[21] FeOOH catalyst (66 kJ/mol),[60] Ni$_{0.35}$Fe$_{0.65}$OOH catalyst (∼30 kJ/mol),[60] Fe$_2$O$_3$ electrode (43−66 kJ/mol),[61] Ni$_{60}$Co$_{40}$ oxides (72.6 kJ/mol),[62] and layered double hydroxides of FeCo (81 kJ/mol).[21] Again, it is consistent with the excellent catalytic activity of FeSe$_2$@CoSe$_2$/rGO-2 observed above for OER.

The OER activities of these selenide catalysts were then normalized with the mass loading of the catalysts. At $\eta = 350$ mV, the mass activity of FeSe$_2$@CoSe$_2$/rGO-2 is calculated to be 727.1 A g^{-1}, which is far superior to those of FeSe$_2$/rGO (3.84 A g^{-1}), FeSe$_2$@CoSe$_2$/rGO-1 (445 A g^{-1}), FeSe$_2$@CoSe$_2$/rGO-3 (164.8 A g^{-1}), and CoSe$_2$/rGO (47.5 A g^{-1}) catalysts (Table 1). To further detect the specific activity of the obtained catalysts and the TOF, the metal ion content in the composites was analyzed with ICP−OES measurements. The result is shown in Table S2 (see the Supporting Information). It was found that the Co/Fe atomic ratios are 0.41:1, 0.88:1, and 1.04:1 for FeSe$_2$@CoSe$_2$/rGO-1, FeSe$_2$@CoSe$_2$/rGO-2, and FeSe$_2$@CoSe$_2$/rGO-3, respectively, in good correlation with the added amount of CoCl$_2$ during sample preparation. The TOF values of the catalysts were also calculated to compare the catalytic performance, which was defined as the number of O$_2$ molecules produced per second per Co or Fe sites. It should be noted that the calculated TOF values are smaller than the actual values because only the metal sites located on the composite surface were involved in the catalytic reaction. One can see that the FeSe$_2$@CoSe$_2$/rGO composites

exhibit much higher TOF values than those of CoSe$_2$/rGO or FeSe$_2$/rGO, based on either cobalt or iron sites.

Figure S10 shows the N$_2$ adsorption/desorption curve of the samples (see the Supporting Information). It can be clearly seen that type IV isotherms with a H3-type hysteresis loop are observed for all products. The Barrett−Joyner−Halenda (BJH) analysis shows that the CoSe$_2$/rGO and FeSe$_2$/rGO products have similar specific surface area (S_{BET} = 6.61 and 6.72 m^2 g^{-1}, respectively). The composites of FeSe$_2$@CoSe$_2$/rGO show specific surface areas in the range of 12.6−23.3 m^2 g^{-1}. At higher CoSe$_2$ loading, the sample exhibits a higher specific surface area. This is consistent with the results of TEM measurement that the reaction of Co^{2+} with FeSe$_2$ induces disintegration of the FeSe$_2$ aggregates forming particles of smaller size. On the basis of these specific surface area values, the area-specific activity, $j/(10S_{BET}m)$, was calculated, which was much higher for FeSe$_2$@CoSe$_2$/rGO-1 (3.54 mA cm^{-2}) and FeSe$_2$@CoSe$_2$/rGO-2 (3.18 mA cm^{-2}) than that for others in the investigated products. It should be noted that the area-specific activity of FeSe$_2$@CoSe$_2$/rGO-3 (0.71 mA cm^{-2}) is similar to that of CoSe$_2$/rGO (0.72 mA cm^{-2}), likely because the surface of FeSe$_2$@CoSe$_2$/rGO-3 is mainly composed of CoSe$_2$.

Considering that not all the surface is electrochemically active, the effective electrochemical surface areas (ECSAs) of the samples were then estimated through electrochemical double-layer capacitance (C_{dl}).[63] The linear relationship between the current density, Δj ($j_a - j_c$), and potential scan rate for the FeSe$_2$@CoSe$_2$/rGO samples is shown in Figure S11 (see Supporting Information), where j_a and j_c are the anodic and cathodic current densities at the middle of the voltage range, respectively. The slopes of the linear regressions, which are two times of C_{dl}, can be used as a representation of ECSA (Figure S11). It can be seen that ECSA does not show the same sequence as that of S_{BET} for the series of samples. Although FeSe$_2$@CoSe$_2$/rGO-2 and FeSe$_2$@CoSe$_2$/rGO-3 have almost the same S_{BET}, the FeSe$_2$@CoSe$_2$/rGO-2 shows a higher ECSA than that of FeSe$_2$@CoSe$_2$/rGO-3. This suggests that only a small part of the FeSe$_2$@CoSe$_2$/rGO-3 surface is electrochemically accessible and the ECSA is mainly contributed by the exposed heterointerfaces between CoSe$_2$ and FeSe$_2$; when with high CoSe$_2$ loadings, the surface is mainly composed of CoSe$_2$, leading to a lower ECSA (FeSe$_2$@CoSe$_2$/rGO-3). The relatively higher ECSA of FeSe$_2$@CoSe$_2$/rGO-2 would also relate to its smaller resistance during the electrocatalytic process. Figure S12 shows electrochemical impedance spectroscopy (EIS) measurement results of the three typical samples, CoSe$_2$/rGO, FeSe$_2$@CoSe$_2$/rGO-2, and FeSe$_2$/rGO. The products of FeSe$_2$/rGO and CoSe$_2$/rGO show a bigger semicircle or a smaller slope, whereas FeSe$_2$@CoSe$_2$/rGO-2

provides almost no semicircle and a higher slope. This indicates a smaller charge-transfer resistance and relatively lower ion diffusion/transport resistance of the FeSe$_2$@CoSe$_2$/rGO-2 catalyst,[64] which is possibly related to the charge-transfer interaction between CoSe$_2$ and FeSe$_2$.

Catalytic Mechanism. As for the detailed catalytic mechanism of water oxidation, at the present stage, there is no consistent viewpoint even for the most usual electrocatalysts, although it is widely accepted that the oxidation process involves the formation of intermediates such as M=O and M—O—O—. For FeCo-based electrocatalysts, some believe that the Co species is the catalytic active sites for OER because Co-based compounds show relatively excellent catalytic performance as compared to Fe-based materials.[25,65] In a nontraditional viewpoint, it is suggested that Fe species are the catalytic active phase, whereas Co-based species in the composite only act as synergic agents, that is, to provide a conductive network for the catalytic process.[52,66] In fact, there is another possibility that both Fe and Co sites are concurrently involved in the catalytic process, the so-called two-site catalytic mechanism.[21] On the basis of the above experimental results, we speculate that cobalt and iron sites are both involved in OER on FeSe$_2$@CoSe$_2$-based catalysts and the catalytic activity is primarily dictated by the heterointerfaces between CoSe$_2$ and FeSe$_2$. A possible OER process on these FeSe$_2$@CoSe$_2$-based catalysts was then proposed and is shown in Figure 8.
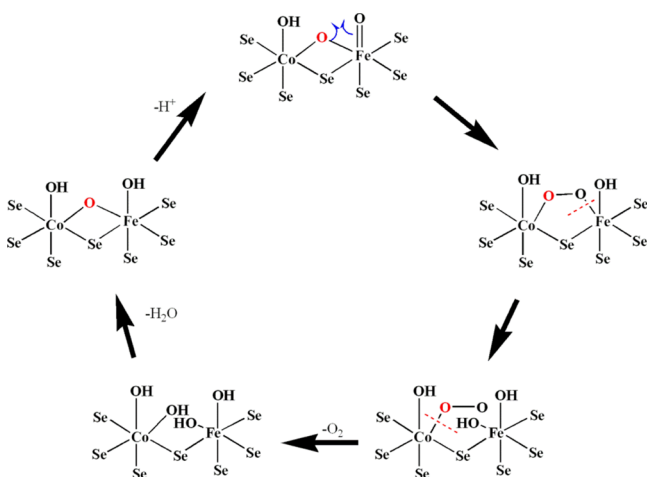

Figure 8. Proposed OER reaction process based on the FeSe$_2$@CoSe$_2$/rGO products.

Both Fe and Co sites in the catalysts are coordinated with six Se in an octahedral configuration. On the surface, the metal sites would be undercoordinated and be bonded with —OH (or H$_2$O) in the electrolyte at high pH. The —OH (or H$_2$O) groups bonded on neighboring metal sites allowed the formation of hydrogen bonds and exchange of protons.[67] The removal of an electron and proton on M—OH induces the formation of M=O oxyl species. In the above XPS measurements (vide ante), results suggest that electron transfer likely occurred from Fe to Co species. This would render the Fe sites to be more acidic (Lewis acid) than the Co sites. Thus, the formation of M=O would preferably be on the Fe sites. The M=O group then evolved toward the formation of O—O bond by germinal coupling with a μ_2-oxygen, forming an —O—O— bridge. Note that the germinal coupling process shows a lower energy barrier than a nucleophilic attack process during

the formation of O—O bond.[68] It is suggested that the resultant M—O—O—M′ linkage can be relatively easily transferred into M—O—O, whereas the intermediate of M—O—O is quite stable (a lifetime of up to 10 ps) according to the theoretical simulation of a Co—O—O configuration.[68]

In the present CoSe$_2$@FeSe$_2$-based catalysts, it is believed that the most important two steps, the formation of M=O and M—O—O—M′, were promoted by the Fe sites with enhanced acidity because of strong charge transfer from Fe and Co. At the same time, the weakened acidity of the cobalt sites would make it easy to break the M—O bond in the stable M—O—O intermediate, thus facilitating the release of O$_2$.[55] In addition, in contrast to conventional oxide catalysts, after the formation of M—O—O intermediates, the generation of dioxygen molecular on selenide catalysts is actually accelerated by the strong 3d—4p repulsion between the metal d-band center and Se p-band center.[29] It should be noted that in our composite catalyst, the involved rGO is also important for the excellent catalytic performance. The involved rGO may not only provide good conductivity but also stabilize the catalytic active composition to prevent them from aggregation.

Application of the FeSe$_2$@CoSe$_2$/rGO Catalyst on a Hematite Photoanode. It is well-known that one of the main challenges in PEC water splitting is the sluggish kinetics of OER, which inhibits the development of PEC systems.[69] Considering the excellent OER performance, the FeSe$_2$@CoSe$_2$/rGO catalysts were then loaded on a hematite photoanode (see Experimental Section for details) for enhanced PEC behavior. The PEC performance of the composite electrode (i.e., the FeSe$_2$@CoSe$_2$/rGO catalyst loaded on a hematite photoanode, denoted as α-Fe$_2$O$_3$//FeSe$_2$@CoSe$_2$/rGO) is presented in Figure 9. For comparison, a bare α-Fe$_2$O$_3$ photoanode was also measured in the same condition. Note that the optimization of the catalyst loading amount on the Fe$_2$O$_3$ photoanode was carried out to ensure best PEC performance, and the optimal loading amount of the FeSe$_2$@CoSe$_2$/rGO-2 catalyst on hematite was identified to be ~0.1 mg/cm^2. Figure 9b shows the LSV plots of bare α-Fe$_2$O$_3$ and α-Fe$_2$O$_3$//FeSe$_2$@CoSe$_2$/rGO composite photoanodes in 1 M KOH electrolyte under light illumination (300 W Xe lamp) or in the dark. At the applied potential of 1.23 versus RHE, the bare hematite electrode yields a photocurrent density of 0.05 mA cm^{-2}, which increased by three-fold to 0.15 mA cm^{-2} after coupling with the FeSe$_2$@CoSe$_2$/rGO-2 catalyst. Thus, three-fold enhancement was obtained upon the loading of the composite catalyst. Additionally, in terms of the photocurrent onset potential, a remarkable cathodic shift is observed from about 1.0 V versus RHE on the bare hematite electrode to 0.7 V versus RHE on the catalyst-loaded hematite electrode. That is, the FeSe$_2$@CoSe$_2$/rGO catalyst greatly accelerated OER on the hematite surface by suppressing interfacial charge recombination, leading to an augment of electron flux and photovoltage.

The photocurrent enhancement after the loading of the FeSe$_2$@CoSe$_2$/rGO-2 catalyst was also probed by the amperometric i—t measurements at the applied potential of 1.4 V versus RHE (Figure 9c) under chopped illumination. Both the pristine α-Fe$_2$O$_3$ and the catalyst-loaded photoanodes showed quick current responses with the light switching on/off. The photocurrent densities were reproducible in the light/dark cycles. The steady-state photocurrent densities of the two electrodes are basically consistent with those under continuous photoirradiation (Figure 9b), indicating that the photocurrent
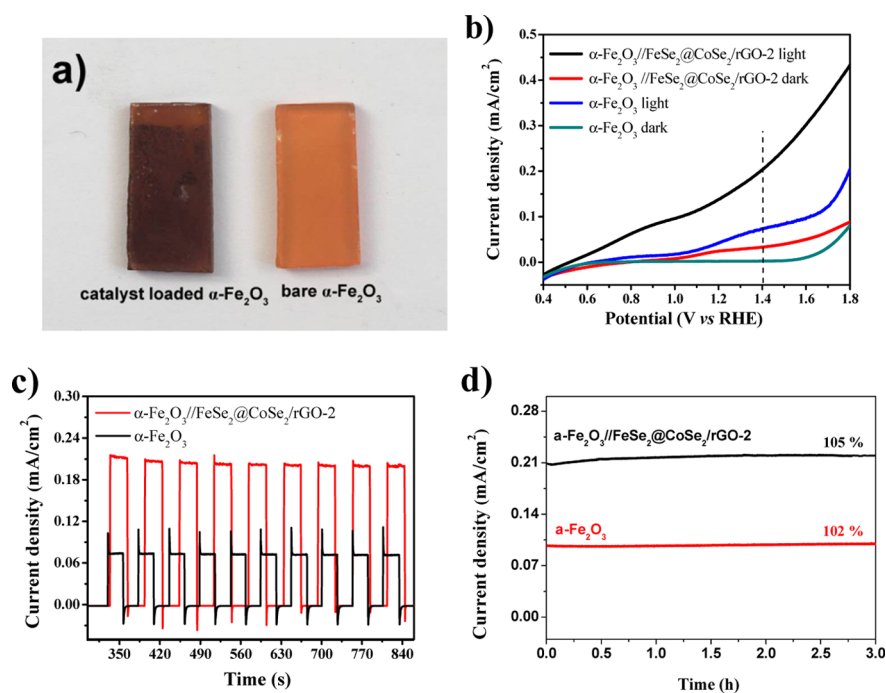
Figure 9. PEC performance tests of the FeSe$_2$@CoSe$_2$/rGO catalyst-loaded hematite photoanodes. (a) Digital image of the hematite photoanodes with or without FeSe$_2$@CoSe$_2$/rGO catalyst and (b) LSV scans recorded under illumination. (c) Amperometric $i-t$ curves plotted at 1.4 V vs RHE under chopped illumination. (d) Amperometric ($i-t$) curves were recorded at a constant applied potential (1.4 V vs RHE) under illumination to evaluate the stabilities of the α-Fe$_2$O$_3$//FeSe$_2$@CoSe$_2$/rGO and pristine α-Fe$_2$O$_3$ photoanodes.

densities are stable without photoinduced charging effect. In addition, the characteristic transient current spikes resulting from the accumulation of photogenerated holes at the semiconductor liquid junction due to the slow OER kinetics were visible on the pristine hematite photoanode. In contrast, these current spikes diminished or disappeared after the catalyst loading, further confirming that the FeSe$_2$@CoSe$_2$/rGO catalyst greatly promoted water oxidation by photogenerated holes, thus avoiding their surface accumulation.[70] The above results demonstrate the impressive enhancement of PEC performance including a greater photocurrent and negative shift of onset potential by the FeSe$_2$@CoSe$_2$/rGO catalyst.

In view of practical use, the durability of the photoelectrode is a crucial major concern. Because of the high oxidative environment originated from the photoinduced holes on the semiconductor surface, OER will compete with the photo-corrosion reaction (i.e., the oxidation of the photoelectrode themselves). In order to probe the durability of the FeSe$_2$@CoSe$_2$/rGO-loaded photoelectrodes, long-term stability tests of the photocurrent density as a function of time were carried out. As shown in Figure 9d, the normalized plots showed that the composite electrode loaded with the prepared catalyst retained 105% of its photocurrent density after 3 h continuous operation. This long-term stability is similar to that of the pristine α-Fe$_2$O$_3$ photoanode (retaining 102% of its photo-current density after 3 h). This further suggests the excellent stability of the catalyst when used on the α-Fe$_2$O$_3$ photoanode.

CONCLUSIONS

In this study, we demonstrate that FeSe$_2$@CoSe$_2$ composites with abundant heterointerfaces can serve as highly efficient electrocatalysts for OER. The FeSe$_2$@CoSe$_2$ composites, in the size range of 50−80 nm, were synthesized and loaded on the rGO surface. The formation of CoSe$_2$ on the FeSe$_2$ surface

induced the disintegration of FeSe$_2$ aggregates, increased ECSA, and introduced abundant heterointerfaces between CoSe$_2$ and FeSe$_2$, which eventually show high catalytic activities toward OER. FeSe$_2$@CoSe$_2$/rGO-2 represents the best catalyst among the series of samples, with a η_{10} of only 260 mV in 1 M KOH and a low onset potential of 1.45 V. It is proposed that the heterointerfaces between CoSe$_2$ on FeSe$_2$ contributed to the remarkable catalytic performance with a two-site mecha-nism. Furthermore, when the catalysts were loaded on a Fe$_2$O$_3$ photoelectrode, the PEC water-splitting performance was markedly enhanced. At the applied potential of 1.23 V versus RHE, the hematite electrode modified with the as-prepared FeSe$_2$@CoSe$_2$/rGO catalyst yielded a photocurrent density of 0.15 mA cm^{-2}, three times that of the bare hematite electrode. Taken together, results from this study suggest a new and effective strategy in the design and engineering of effective OER electrocatalysts and their potential application in photo-electrolysis-driven water splitting.

ASSOCIATED CONTENT

⬡ Supporting Information

The Supporting Information is available free of charge on the ACS Publications website at DOI: 10.1021/acsami.8b04024.

> XPS survey scan of the FeSe$_2$@CoSe$_2$/rGO product; detailed XPS spectrum of C 1s and Se 3d; XPS spectra of the catalysts after OER testing; Raman spectra of some hybrid products; SEM and TEM images of FeSe$_2$/rGO and FeSe$_2$@CoSe$_2$/rGO products; LSV curves collected in 0.1 M KOH solution and the corresponding Tafel slopes; EIS measurement of the three contrast catalysts; investigation of the Faradic efficiency; N$_2$ adsorption−desorption isotherms and comparison of the specific surface area for the investigated samples; cyclic voltammogram curves and curves of charging current

density differences versus scanning rates; comparison of OER activities for various noble metal-free OER catalysts; and ICP−OES analysis results of FeSe$_2$@CoSe$_2$/rGO products (PDF)

■ AUTHOR INFORMATION

Corresponding Authors
*E-mail: zhuguoxing@ujs.edu.cn (G.Z.).
*E-mail: xiaopingshen@ujs.edu.cn (X.S.).
*E-mail: shaowei@ucsc.edu (S.C.).
ORCID
Guoxing Zhu: 0000-0002-0756-7451
Xiaoping Shen: 0000-0003-0366-6433
Shaowei Chen: 0000-0002-3668-8551
Notes
The authors declare no competing financial interest.

■ ACKNOWLEDGMENTS

■ REFERENCES

(1) Walter, M. G.; Warren, E. L.; McKone, J. R.; Boettcher, S. W.; Mi, Q.; Santori, E. A.; Lewis, N. S. Solar Water Splitting Cells. *Chem. Rev.* **2010**, *110*, 6446−6473.

(2) Zhang, W.; Lai, W.; Cao, R. Energy-related Small Molecule Activation Reactions: Oxygen Reduction and Hydrogen and Oxygen Evolution Reactions Catalyzed by Porphyrin- and Corrole-based Systems. *Chem. Rev.* **2017**, *117*, 3717−3797.

(3) Suen, N.-T.; Hung, S.-F.; Quan, Q.; Zhang, N.; Xu, Y.-J.; Chen, H. M. Electrocatalysis for the Oxygen Evolution Reaction: Recent Development and Future Perspectives. *Chem. Soc. Rev.* **2017**, *46*, 337−365.

(4) Wang, J.; Zhong, H.-x.; Qin, Y.-l.; Zhang, X.-b. An Efficient Three-dimensional Oxygen Evolution Electrode. *Angew. Chem., Int. Ed.* **2013**, *52*, 5248−5253.

(5) Okamura, M.; Kondo, M.; Kuga, R.; Kurashige, Y.; Yanai, T.; Hayami, S.; Praneeth, V. K. K.; Yoshida, M.; Yoneda, K.; Kawata, S.; Masaoka, S. A Pentanuclear Iron Catalyst Designed for Water Oxidation. *Nature* **2016**, *530*, 465−468.

(6) Stamenkovic, V. R.; Strmcnik, D.; Lopes, P. P.; Markovic, N. M. Energy and Fuels from Electrochemical Interfaces. *Nat. Mater.* **2016**, *16*, 57−69.

(7) Paoli, E. A.; Masini, F.; Frydendal, R.; Deiana, D.; Schlaup, C.; Malizia, M.; Hansen, T. W.; Horch, S.; Stephens, I. E. L.; Chorkendorff, I. Oxygen Evolution on Well-characterized Mass-selected Ru and RuO$_2$ Nanoparticles. *Chem. Sci.* **2015**, *6*, 190−196.

(8) Lee, Y.; Suntivich, J.; May, K. J.; Perry, E. E.; Shao-Horn, Y. Synthesis and Activities of Rutile IrO$_2$ and RuO$_2$ Nanoparticles for Oxygen Evolution in Acid and Alkaline Solutions. *J. Phys. Chem. Lett.* **2012**, *3*, 399−404.

(9) Burke, M. S.; Zou, S.; Enman, L. J.; Kellon, J. E.; Gabor, C. A.; Pledger, E.; Boettcher, S. W. Revised Oxygen Evolution Reaction Activity Trends for First-row Transition-metal (Oxy)hydroxides in Alkaline Media. *J. Phys. Chem. Lett.* **2015**, *6*, 3737−3742.

(10) Han, L.; Dong, S.; Wang, E. Transition-metal (Co, Ni, and Fe)-based Electrocatalysts for the Water Oxidation Reaction. *Adv. Mater.* **2016**, *28*, 9266−9291.

(11) Chen, M.; Wu, Y.; Han, Y.; Lin, X.; Sun, J.; Zhang, W.; Cao, R. An Iron-based Film for Highly Efficient Electrocatalytic Oxygen Evolution from Neutral Aqueous Solution. *ACS Appl. Mater. Interfaces* **2015**, *7*, 21852−21859.

(12) Chen, C.; Ciucci, F. Designing Fe-based Oxygen Catalysts by Density Functional Theory Calculations. *Chem. Mater.* **2016**, *28*, 7058−7065.

(13) Gao, M.-R.; Cao, X.; Gao, Q.; Xu, Y.-F.; Zheng, Y.-R.; Jiang, J.; Yu, S.-H. Nitrogen-Doped Graphene Supported CoSe$_2$ Nanobelt Composite Catalyst for Efficient Water Oxidation. *ACS Nano* **2014**, *8*, 3970−3978.

(14) Wu, G.; Santandreu, A.; Kellogg, W.; Gupta, S.; Ogoke, O.; Zhang, H.; Wang, H.-L.; Dai, L. Carbon Nanocomposite Catalysts for Oxygen Reduction and Evolution Reactions: from Nitrogen Doping to Transition-metal Addition. *Nano Energy* **2016**, *29*, 83−110.

(15) Jiao, Y.; Zheng, Y.; Davey, K.; Qiao, S.-Z. Activity Origin and Catalyst Design Principles for Electrocatalytic Hydrogen Evolution on Heteroatom-doped Graphene. *Nat. Energy* **2016**, *1*, 16130.

(16) Friebel, D.; Louie, M. W.; Bajdich, M.; Sanwald, K. E.; Cai, Y.; Wise, A. M.; Cheng, M.-J.; Sokaras, D.; Weng, T.-C.; Alonso-Mori, R.; Davis, R. C.; Bargar, J. R.; Nørskov, J. K.; Nilsson, A.; Bell, A. T. Identification of Highly Active Fe Sites in (Ni, Fe)OOH for Electrocatalytic Water Splitting. *J. Am. Chem. Soc.* **2015**, *137*, 1305−1313.

(17) Zhao, S.; Li, M.; Han, M.; Xu, D.; Yang, J.; Lin, Y.; Shi, N.-E.; Lu, Y.; Yang, R.; Liu, B.; Dai, Z.; Bao, J. Defect-rich Ni$_3$FeN Nanocrystals Anchored on N-doped Graphene for Enhanced Electrocatalytic Oxygen Evolution. *Adv. Funct. Mater.* **2018**, *28*, 1706018.

(18) Li, M.; Xiong, Y.; Liu, X.; Bo, X.; Zhang, Y.; Han, C.; Guo, L. Facile Synthesis of Electrospun MFe$_2$O$_4$ (M = Co, Ni, Cu, Mn) Spinel Nanofibers with Excellent Electrocatalytic Properties for Oxygen Evolution and Hydrogen Peroxide Reduction. *Nanoscale* **2015**, *7*, 8920−8930.

(19) Long, X.; Li, J.; Xiao, S.; Yan, K.; Wang, Z.; Chen, H.; Yang, S. Strongly Coupled Graphene and FeNi Double Hydroxide Hybrid as an Excellent Electrocatalyst for the Oxygen Evolution Reaction. *Angew. Chem., Int. Ed.* **2014**, *53*, 7584−7588.

(20) You, C.; Ji, Y.; Liu, Z.; Xiong, X.; Sun, X. Ultrathin CoFe-borate Layer Coated CoFe-layered Double Hydroxide Nanosheets Array: a Non-noble-metal 3D Catalyst Electrode for Efficient and Durable Water Oxidation in Potassium Borate. *ACS Sustainable Chem. Eng.* **2018**, *6*, 1527−1531.

(21) Zhang, B.; Zheng, X.; Voznyy, O.; Comin, R.; Bajdich, M.; Garcia-Melchor, M.; Han, L.; Xu, J.; Liu, M.; Zheng, L.; de Arquer, F. P. G.; Dinh, C. T.; Fan, F.; Yuan, M.; Yassitepe, E.; Chen, N.; Regier, T.; Liu, P.; Li, Y.; De Luna, P.; Janmohamed, A.; Xin, H. L.; Yang, H.; Vojvodic, A.; Sargent, E. H. Homogeneously Dispersed Multimetal Oxygen-evolving Catalyst. *Science* **2016**, *352*, 333−337.

(22) Yang, N.; Tang, C.; Wang, K.; Du, G.; Asiri, A. M.; Sun, X. Iron-doped Nickel Disulfide Nanoarray: A Highly Efficient and Stable Electrocatalyst for Water Splitting. *Nano Res.* **2016**, *9*, 3346−3354.

(23) Vlamidis, Y.; Scavetta, E.; Gazzano, M.; Tonelli, D. Iron vs Aluminum Based Layered Double Hydroxides as Water Splitting Catalysts. *Electrochim. Acta* **2016**, *188*, 653−660.

(24) Li, B.-Q.; Zhang, S.-Y.; Tang, C.; Cui, X.; Zhang, Q. Anionic Regulated NiFe (Oxy)sulfide Electrocatalysts for Water Oxidation. *Small* **2017**, *13*, 1700610.

(25) Liu, W.; Liu, H.; Dang, L.; Zhang, H.; Wu, X.; Yang, B.; Li, Z.; Zhang, X.; Lei, L.; Lin, S. Amorphous Cobalt-iron Hydroxide Nanosheet Electrocatalyst for Efficient Electrochemical and Photo-electrochemical Oxygen Evolution. *Adv. Funct. Mater.* **2017**, *27*, 1603904.

(26) Shen, M.; Ruan, C.; Chen, Y.; Jiang, C.; Ai, K.; Lu, L. Covalent Entrapment of Cobalt-iron Sulfides in N-doped Mesoporous Carbon: Extraordinary Bifunctional Electrocatalysts for Oxygen Reduction and Evolution Reactions. *ACS Appl. Mater. Interfaces* **2015**, *7*, 1207−1218.

(27) Zhang, J.-Y.; Lv, L.; Tian, Y.; Li, Z.; Ao, X.; Lan, Y.; Jiang, J.; Wang, C. Rational Design of Cobalt-iron Selenides for Highly Efficient Electrochemical Water Oxidation. *ACS Appl. Mater. Interfaces* **2017**, *9*, 33833−33840.

(28) Chi, J.-Q.; Shang, X.; Gao, W.-K.; Dong, B.; Yan, K.-L.; Li, X.; Liu, Y.-R.; Chai, Y.-M.; Liu, C.-G. Binary Metal Fe$_{0.5}$Co$_{0.5}$Se$_2$ Spheres

Supported on Carbon Fiber Cloth for Efficient Oxygen Evolution Reaction. *Int. J. Hydrogen Energy* **2017**, *42*, 15189−15195.

(29) Anantharaj, S.; Ede, S. R.; Sakthikumar, K.; Karthick, K.; Mishra, S.; Kundu, S. Recent Trends and Perspectives in Electrochemical Water Splitting with an Emphasis to Sulphide, Selenide and Phosphide Catalysts of Fe, Co and Ni: a Review. *ACS Catal.* **2016**, *6*, 8069−8097.

(30) Yu, J.; Cheng, G.; Luo, W. 3D Mesoporous Rose-like Nickel-iron Selenide Microspheres as Advanced Electrocatalysts for the Oxygen Evolution Reaction. *Nano Res.* **2018**, *11*, 2149−2158.

(31) Du, Y.; Cheng, G.; Luo, W. NiSe$_2$/FeSe$_2$ Nanodendrites: a Highly Efficient Electrocatalyst for Oxygen Evolution Reaction. *Catal. Sci. Technol.* **2017**, *7*, 4604−4608.

(32) Du, Y.; Cheng, G.; Luo, W. Colloidal Synthesis of Urchin-like Fe Doped NiSe$_2$ for Efficient Oxygen Evolution. *Nanoscale* **2017**, *9*, 6821−6825.

(33) Li, X.; Zhang, L.; Huang, M.; Wang, S.; Li, X.; Zhu, H. Cobalt and Nickel Selenide Nanowalls Anchored on Graphene as Bifunctional Electrocatalysts for Overall Water Splitting. *J. Mater. Chem. A* **2016**, *4*, 14789−14795.

(34) Cui, X.; Ren, P.; Deng, D.; Deng, J.; Bao, X. Single Layer Graphene Encapsulating Non-precious Metals as High-performance Electrocatalysts for Water Oxidation. *Energy Environ. Sci.* **2016**, *9*, 123−129.

(35) Li, C.; Wang, T.; Luo, Z.; Liu, S.; Gong, J. Enhanced Charge Separation through ALD-modified Fe$_2$O$_3$/Fe$_2$TiO$_5$ Nanorod Heterojunction for Photoelectrochemical Water Oxidation. *Small* **2016**, *12*, 3415−3422.

(36) Qiu, Y.; Xin, L.; Li, W. Electrocatalytic Oxygen Evolution over Supported Small Amorphous Ni-Fe Nanoparticles in Alkaline Electrolyte. *Langmuir* **2014**, *30*, 7893−7901.

(37) Paulus, U. A.; Schmidt, T. J.; Gasteiger, H. A.; Behm, R. J. Oxygen Reduction on a High-surface Area Pt: Vulcan Carbon Catalyst: a Thin-film Rotating Ring-disk Electrode Study. *J. Electroanal. Chem.* **2001**, *495*, 134−145.

(38) McCrory, C. C. L.; Jung, S.; Peters, J. C.; Jaramillo, T. F. Benchmarking Heterogeneous Electrocatalysts for the Oxygen Evolution Reaction. *J. Am. Chem. Soc.* **2013**, *135*, 16977−16987.

(39) Lu, X.; Zhao, C. Electrodeposition of Hierarchically Structured Three- dimensional Nickel-iron Electrodes for Efficient Oxygen Evolution at High Current Densities. *Nat. Commun.* **2015**, *6*, 6616.

(40) Zhu, G.; Xi, C.; Liu, Y.; Zhu, J.; Shen, X. CN Foam Loaded with Few-layer Graphene Nanosheets for High-performance Supercapacitor Electrodes. *J. Mater. Chem. A* **2015**, *3*, 7591−7599.

(41) Gao, R.; Zhang, H.; Yan, D. Iron Diselenide Nanoplatelets: Stable and Efficient Water-electrolysis Catalysts. *Nano Energy* **2017**, *31*, 90−95.

(42) Yang, J.; Zhu, G.; Liu, Y.; Xia, J.; Ji, Z.; Shen, X.; Wu, S. Fe$_3$O$_4$-Decorated Co$_9$S$_8$ Nanoparticles In situ Grown on Reduced Graphene Oxide: a New and Efficient Electrocatalyst for Oxygen Evolution Reaction. *Adv. Funct. Mater.* **2016**, *26*, 4712−4721.

(43) van der Heide, H.; Hemmel, R.; van Bruggen, C. F.; Haas, C. X-ray Photoelectron Spectra of 3d Transition Metal Pyrites. *J. Solid State Chem.* **1980**, *33*, 17−25.

(44) Liu, Y.; Cheng, H.; Lyu, M.; Fan, S.; Liu, Q.; Zhang, W.; Zhi, Y.; Wang, C.; Xiao, C.; Wei, S.; Ye, B.; Xie, Y. Low Overpotential in Vacancy-rich Ultrathin CoSe$_2$ Nanosheets for Water Oxidation. *J. Am. Chem. Soc.* **2014**, *136*, 15670−15675.

(45) Xu, X.; Ge, Y.; Wang, W.; Zhang, Z.; Dong, P.; Baines, R.; Ye, M.; Shen, J. Cobalt-doped FeSe$_2$-RGO as Highly Active and Stable Electrocatalysts for Hydrogen Evolution Reactions. *ACS Appl. Mater. Interfaces* **2016**, *8*, 18036−18042.

(46) Huang, S.; He, Q.; Chen, W.; Qiao, Q.; Zai, J.; Qian, X. Ultrathin FeSe$_2$ Nanosheets: Controlled Synthesis and Application as a Heterogeneous Catalyst in Dye-sensitized Solar Cells. *Chem.—Eur. J.* **2015**, *21*, 4085−4091.

(47) Xia, C.; Jiang, Q.; Zhao, C.; Hedhili, M. N.; Alshareef, H. N. Selenide-based Electrocatalysts and Scaffolds for Water Oxidation Applications. *Adv. Mater.* **2016**, *28*, 77−85.

(48) Hang, L.; Sun, Y.; Men, D.; Liu, S.; Zhao, Q.; Cai, W.; Li, Y. Hierarchical Micro/nanostructured C Doped Co/Co3O4 Hollow Spheres Derived from PS@Co(OH)2 for the Oxygen Evolution Reaction. *J. Mater. Chem. A* **2017**, *5*, 11163−11170.

(49) Tabassum, H.; Guo, W.; Meng, W.; Mahmood, A.; Zhao, R.; Wang, Q.; Zou, R. Metal-organic Frameworks Derived Cobalt Phosphide Architecture Encapsulated into B/N Co-doped Graphene Nanotubes for All pH Value Electrochemical Hydrogen Evolution. *Adv. Energy Mater.* **2017**, *7*, 1601671.

(50) Lu, Z.; Wang, H.; Kong, D.; Yan, K.; Hsu, P.-C.; Zheng, G.; Yao, H.; Liang, Z.; Sun, X.; Cui, Y. Electrochemical Tuning of Layered Lithium Transition Metal Oxides for Improvement of Oxygen Evolution Reaction. *Nat. Commun.* **2014**, *5*, 4345.

(51) Han, X.; Yu, C.; Yang, J.; Zhao, C.; Huang, H.; Liu, Z.; Ajayan, P. M.; Qiu, J. Mass and Charge Transfer Coenhanced Oxygen Evolution Behaviors in CoFe-layered Double Hydroxide Assembled on Graphene. *Adv. Mater. Interfaces* **2016**, *3*, 1500782.

(52) Burke, M. S.; Kast, M. G.; Trotochaud, L.; Smith, A. M.; Boettcher, S. W. Cobalt-iron (Oxy)hydroxide Oxygen Evolution Electrocatalysts: the Role of Structure and Composition on Activity, Stability, and Mechanism. *J. Am. Chem. Soc.* **2015**, *137*, 3638−3648.

(53) Zhuang, L.; Ge, L.; Yang, Y.; Li, M.; Jia, Y.; Yao, X.; Zhu, Z. Ultrathin Iron-cobalt Oxide Nanosheets with Abundant Oxygen Vacancies for the Oxygen Evolution Reaction. *Adv. Mater.* **2017**, *29*, 1606793.

(54) Doyle, R. L.; Godwin, I. J.; Brandon, M. P.; Lyons, M. E. G. Redox and Electrochemical Water Splitting Catalytic Properties of Hydrated Metal Oxide Modified Electrodes. *Phys. Chem. Chem. Phys.* **2013**, *15*, 13737−13783.

(55) Risch, M.; Ringleb, F.; Kohlhoff, M.; Bogdanoff, P.; Chernev, P.; Zaharieva, I.; Dau, H. Water Oxidation by Amorphous Cobalt-based Oxides: In situ Tracking of Redox Transitions and Mode of Catalysis. *Energy Environ. Sci.* **2015**, *8*, 661−674.

(56) Bajdich, M.; García-Mota, M.; Vojvodic, A.; Nørskov, J. K.; Bell, A. T. Theoretical Investigation of the Activity of Cobalt Oxides for the Electrochemical Oxidation of Water. *J. Am. Chem. Soc.* **2013**, *135*, 13521−13530.

(57) Liu, T.; Asiri, A. M.; Sun, X. Electrodeposited Co-doped NiSe$_2$ Nanoparticles Film: a Good Electrocatalyst for Efficient Water Splitting. *Nanoscale* **2016**, *8*, 3911−3915.

(58) Wang, Z.; Li, J.; Tian, X.; Wang, X.; Yu, Y.; Owusu, K. A.; He, L.; Mai, L. Porous Nickel-iron Selenide Nanosheets as Highly Efficient Electrocatalysts for Oxygen Evolution Reaction. *ACS Appl. Mater. Interfaces* **2016**, *8*, 19386−19392.

(59) Danilovic, N.; Subbaraman, R.; Chang, K.-C.; Chang, S. H.; Kang, Y. J.; Snyder, J.; Paulikas, A. P.; Strmcnik, D.; Kim, Y.-T.; Myers, D.; Stamenkovic, V. R.; Markovic, N. M. Activity-Stability Trends for the Oxygen Evolution Reaction on Monometallic Oxides in Acidic Environments. *J. Phys. Chem. Lett.* **2014**, *5*, 2474−2478.

(60) Swierk, J. R.; Klaus, S.; Trotochaud, L.; Bell, A. T.; Tilley, T. D. Electrochemical Study of the Energetics of the Oxygen Evolution Reaction at Nickel Iron (Oxy)hydroxide Catalysts. *J. Phys. Chem. C* **2015**, *119*, 19022−19029.

(61) Cowan, A. J.; Barnett, C. J.; Pendlebury, S. R.; Barroso, M.; Sivula, K.; Grätzel, M.; Durrant, J. R.; Klug, D. R. Activation Energies for the Rate-limiting Step in Water Photooxidation by Nanostructured α-Fe$_2$O$_3$ and TiO$_2$. *J. Am. Chem. Soc.* **2011**, *133*, 10134−10140.

(62) Rosalbino, F.; Delsante, S.; Borzone, G.; Scavino, G. Electrocatalytic Activity of Crystalline Ni-Co-M (M = Cr, Mn, Cu) Alloys on the Oxygen Evolution Reaction in an Alkaline Environment. *Int. J. Hydrogen Energy* **2013**, *38*, 10170−10177.

(63) Song, F.; Hu, X. Ultrathin Cobalt-manganese Layered Double Hydroxide is an Efficient Oxygen Evolution Catalyst. *J. Am. Chem. Soc.* **2014**, *136*, 16481−16484.

(64) Xi, C.; Zhu, G.; Liu, Y.; Shen, X.; Zhu, W.; Ji, Z.; Kong, L. Belt-like Nickel Hydroxide Carbonate/reduced Graphene Oxide Hybrids: Synthesis and Performance as Supercapacitor Electrodes. *Colloids Surf., A* **2018**, *538*, 748−756.

(65) Geng, J.; Kuai, L.; Kan, E.; Wang, Q.; Geng, B. Precious-metal-free Co-Fe-O/rGO Synergetic Electrocatalysts for Oxygen Evolution Reaction by a Facile Hydrothermal Route. *ChemSusChem* **2015**, *8*, 659−664.

(66) Bates, M. K.; Jia, Q.; Doan, H.; Liang, W.; Mukerjee, S. Charge-transfer Effects in Ni-Fe and Ni-Fe-Co Mixed-metal Oxides for the Alkaline Oxygen Evolution Reaction. *ACS Catal.* **2016**, *6*, 155−161.

(67) Mattioli, G.; Risch, M.; Bonapasta, A. A.; Dau, H.; Guidoni, L. Protonation States in a Cobalt-oxide Catalyst for Water Oxidation: Fine Comparison of Ab initio Molecular Dynamics and X-ray Absorption Spectroscopy Results. *Phys. Chem. Chem. Phys.* **2011**, *13*, 15437−15441.

(68) Mattioli, G.; Giannozzi, P.; Bonapasta, A. A.; Guidoni, L. Reaction Pathways for Oxygen Evolution Promoted by Cobalt Catalyst. *J. Am. Chem. Soc.* **2013**, *135*, 15353−15363.

(69) Chen, H. M.; Chen, C. K.; Liu, R.-S.; Zhang, L.; Zhang, J.; Wilkinson, D. P. Nanoarchitecture and Material Designs for Water Splitting Photoelectrodes. *Chem. Soc. Rev.* **2012**, *41*, 5654−5671.

(70) Bao, C.; Zhu, G.; Yang, J.; Liu, M.; Zhang, R.; Shen, X. Small Molecular Amine Mediated Synthesis of Hydrophilic CdS Nanorods and their Photoelectrochemical Water Splitting Performance. *Dalton Trans.* **2015**, *44*, 1465−1472.